Fluctuation Methods To Study Protein Aggregation in Live Cells: Concanavalin A Oligomers Formation

V. Vetri,[†] G. Ossato,[‡] V. Militello,[†] M. A. Digman,[‡] M. Leone,[†] and E. Gratton[‡*]
[†]Dipartimento di Scienze Fisiche ed Astronomiche, University of Palermo, Palermo, Italy; and [‡]Laboratory for Fluorescence Dynamics, University of California, Irvine, California

ABSTRACT Prefibrillar oligomers of proteins are suspected to be the primary pathogenic agents in several neurodegenerative diseases. A key approach for elucidating the pathogenic mechanisms is to probe the existence of oligomers directly in living cells. In this work, we were able to monitor the process of aggregation of Concanavalin A in live cells. We used number and brightness analysis, two-color cross number and brightness analysis, and Raster image correlation spectroscopy to obtain the number of molecules, aggregation state, and diffusion coefficient as a function of time and cell location. We observed that binding of Concanavalin A to the membrane and the formation of small aggregates paralleled cell morphology changes, indicating progressive cell compaction and death. Upon protein aggregation, we observed increased membrane water penetration as reported by Laurdan generalized polarization imaging.

INTRODUCTION

A number of human diseases are associated with protein aggregation processes and, in particular, fibril formation. Understanding how and when this occurs remains one of the greatest challenges in this area of biophysical and biomedical science (1–3). It is known that protein conversion into a nonnative conformation is the initial trigger of the aggregation process associated with these pathologies (4). Under the appropriate conditions, proteins can convert into amyloid-like structures (5), and despite the absence of any sequence or structural homologies in native proteins or peptides, the oligomers and fibrils that result from aggregation are structurally similar. This suggests that common principles regulate both correct protein folding and aggregation (5). In addition, the fact that protein aggregates that are not related to amyloidoses are cytotoxic, and the strict analogy between the behavior of cells in culture treated with misfolded nonpathogenic proteins and cells in pathogenic conditions suggest a common mechanism for cytotoxicity (1). The mechanisms leading to the formation of amyloidal structures and their relationship with neurodegenerative diseases are still unclear. There is debate about whether prefibrillar oligomers (1,6,7) or fibrils alone are the prime toxic agents (8,9), and small, transient prefibrillar oligomers are often considered to initiate cell death (10–12). This issue is further complicated by the recent observation that cell death is induced by a continuum of cross-β-sheet-containing aggregates rather than by a single uniform species (9,13). Moreover, there is evidence that protein conversion into toxic aggregates is enhanced by membrane interactions (14). The hypothesis that cytotoxicity is related to aggregation at the membrane requires more investigation and validation in the cellular environment (15). A better understanding of the cytotoxicity mechanisms and the role of intermediate species can be achieved by following protein aggregation in time, so that the size of the aggregates can be determined when the changes in cell morphology and membrane properties appear.

Concanavalin A (ConA) is the most extensively studied member of the *lectin* family. It selectively cross-links cell surface glycoproteins and exerts profound effects on mammalian cells, including the initiation of cell agglutination, mitogenesis, and apoptosis. This protein has been found to be toxic to several tumor cell lines, and its antitumor activity has been the topic of recent studies (16–19). ConA has been reported to induce programmed cell death (PCD) on cortical neurons by a mechanism that displays remarkable analogies to PCD induced by the amyloid β peptide, which is universally known for its role in Alzheimer's disease (17,20).

In vitro, ConA readily forms fibrils involving secondary structure changes that lead to β-aggregate structures (21,22), and fibrillar formation is observed under physiological conditions. Together with the rapid formation of fibrillar structures, the high repeatability of the aggregation kinetics, and the morphology of the final aggregates, this makes ConA a good model for studying protein aggregation in live cells. Recent results have shown that the extracellular addition of native or oligomeric ConA on human neuroblastoma cells causes cell death via an extrinsic apoptotic pathway, whereas mature fibrils are essentially harmless (23). It was speculated that oligomer interactions with the cell membrane could cause damage to the structural organization, and that the formation of cross-β-sheet-containing aggregates is involved in this process (23).

In this work, we used number and brightness (N&B) fluctuation spectroscopy analysis (24,25) and its cross-variance (26) to directly follow the aggregation kinetics of ConA

Submitted August 25, 2010, and accepted for publication November 29, 2010.

*Correspondence: egratton22@yahoo.com

Editor: Laura Finzi.

0006-3495/11/02/0774/10 $2.00

doi: 10.1016/j.bpj.2010.11.089

after extracellular addition to live-cell cultures. A map of localized protein aggregations of the protein on the membrane of the live cell was obtained and the average size of the protein aggregates was determined (24,26,27). To confirm protein membrane binding, we used the Raster image correlation spectroscopy (RICS) technique (28–32). RICS provides information about the diffusion and binding to the cell membrane of molecules and, in particular, small ConA aggregates that are formed close to the membrane. Our results establish the kinetics and the degree of ConA oligomerization directly in living cells. They also show the location of protein aggregation, which occurs at the membrane, and the changes in membrane structure induced by ConA aggregation, providing a possible explanation for the cytotoxicity of this protein. We used the membrane probe Laurdan (33–37) to explore changes in the physical properties of the cell membrane that occurred after extracellular addition of ConA. The time evolution of generalized polarization (GP), which quantifies the progressive shift in the position of the Laurdan spectrum, provides a relative measure of increased water penetration in the membrane and the resulting structural destabilization. This alteration of membrane organization is also reported by the Annexin V test and can be related to early events of apoptosis.

MATERIALS AND METHODS

A detailed description of the materials and methods used in this work, including the cell culture and microscopy, can be found in the Supporting Material. In brief, we performed confocal microscopy with a commercial microscope (Olympus Fluoview 1000; Olympus, Tokyo, Japan) and applied image fluctuation spectroscopy methods (N&B and RICS) to obtain information about the state of aggregation and diffusion of labeled ConA in the cells and the surrounding media. We performed the N&B and cross-N&B analyses using the SimFCS program (Laboratory for Fluorescence Dynamics, University of California, Irvine, CA) as previously described (24–27,30). The calibration plots used for the quantitative analysis of the brightness and cross-brightness are reported in Fig. S1 and Fig. S2, respectively. The calibration for single-color N&B (Fig. S1) gives an apparent brightness of B = 1.12 that is taken in account as the apparent brightness of the native ConA tetramer. The calibration for cross-N&B (Fig. S2) gives two values of apparent brightness for the unit (defined as the element of minimum brightness), which in this experiment is associated to the ConA tetramer. The unit resulted in $B_1 = 1.09$ for ConA-Alexa488 in the green channel and $B_2 = 1.12$ for ConA-Alexa647 in the red channel. To determine membrane water penetration, we used the Laurdan GP approach. A full discussion about the use and mathematical significance of GP can be found in the literature (33–37).

RESULTS

Aggregation kinetics in live cells: N&B analysis

Mouse embryonic fibroblast (MEF) cells were observed as a function of time after extracellular addition of ConA-Alexa647. Image stacks were acquired at 10, 25, 45, 60, 75, and 100 min after ConA extracellular addition. In Fig. 1 we show the B-versus-intensity two-dimensional (2D) histogram obtained for the first image stack (*a*), the B histogram (*b*), and the N histogram (*c*), in which the total number of pixels (*y* axis) is plotted versus B and versus N, respectively.

In contrast to the calibration plot, where a single-pixel distribution is observed (Fig. S1), the N&B map in Fig. 1 is broadly distributed, highlighting the intrinsic heterogeneity of the sample. The 2D histogram presents a tail elongated toward higher intensities, i.e., these pixels have a higher number of fluorescent molecules. By selecting

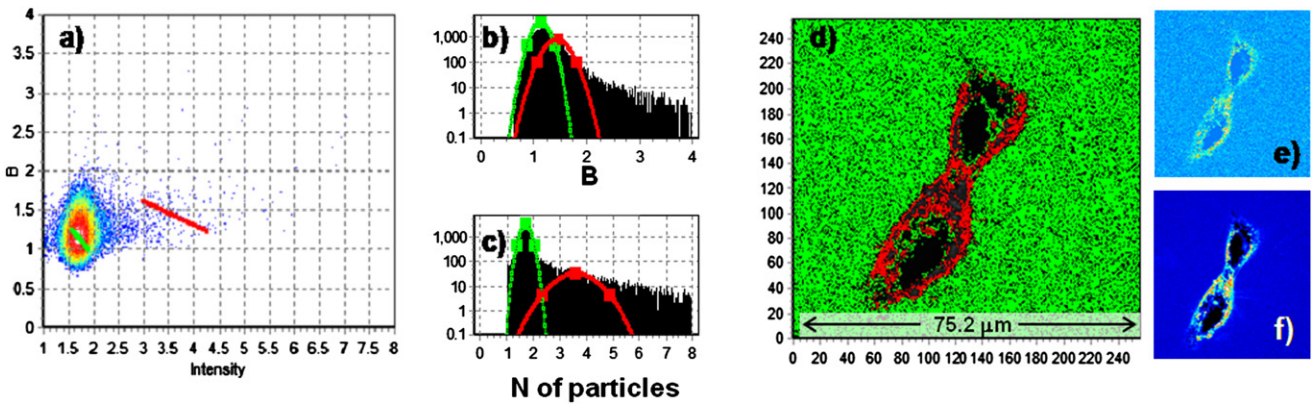

FIGURE 1 (*a*) B versus intensity 2D histogram from N&B analysis of an image stack acquired 10 min after ConA addition. The green segment shows particles with B = 1.12, and the red segment shows particles with slightly higher B and higher intensity. (*b*) B histogram. The red and green lines are used to select two distributions of pixels with different average B-values; these lines show two main populations of molecules with different aggregation states. The green line indicates pixels with average B = 1.12 corresponding to nonaggregated ConA, and the red line indicates pixels with average B = 1.32 corresponding to small oligomers. (*c*) N histogram. The red and green lines are used to select the same two main populations of fluorescent molecules visualized in panels *a* and *b*. The distributions indicated by the green and red lines are characterized by different ConA concentrations. (*d*) Binary selection map. Colored points indicate pixels corresponding to the red and green selections. Pixels with average B = 1.12 and low concentrations are located in the medium away from the cell (*green*), whereas pixels with average B = 1.32 and higher concentrations are located at the membrane (*red*). (*e*) B map (color scale ranges from 0 to 4). (*f*) Average intensity map (color scale ranges from 1 to 8).

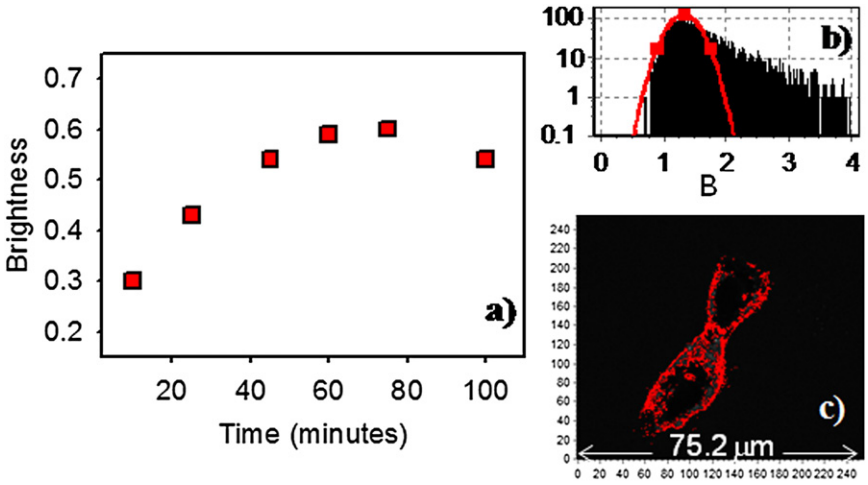

FIGURE 2 (*a*) Time evolution of B1 values of aggregating ConA molecules at the cell membrane. The values are measured as the average brightness of the pixel distribution with higher intensity (red distribution). We use the B1-value to quickly visualize aggregation, since the aggregate size can be found as the ratio $(B_{aggregate}\text{-}1)/(B_{unit}\text{-}1)$ (24,25). (*b*) B histogram of pixels with intensity > 2.2 for the data set at 10 min. For each data set, pixels in the large values of B of the B versus intensity map were isolated, and the time evolution of their brightness (selected by the *red line*) was followed. (*c*) Binary selection map; red points indicate the pixels corresponding to the red reference line. All of these pixels, with average brightness of 1.32, are located at the cell membrane.

these pixels (e.g., pixels with intensity > 2.2), we can see that they are located at the cell membrane, thus indicating a higher local concentration of labeled molecules in this location. Moreover, a few pixels with higher intensity have brightness larger than this value. This suggests the formation of aggregates at the membrane.

In Fig. 1, *b* and *c*, the B and N histograms are reported. Fig. 1 *b* shows a broad distribution of B with respect to the reference plot ($B = 1.12$ from calibration) of nonaggregated protein. The number and brightness histograms show the presence of at least two distributions of pixels, indicating the presence of two populations of molecules. The pixels in these distributions are indicated in Fig. 1, *a–c*, by green and red lines. The green line selects pixels with fewer molecules and identifies an apparent brightness distribution centered at $B = 1.12$, which is consistent with the B-value found for nonaggregated protein by the calibration procedure. The red line selects pixels with higher N and higher B, indicating the presence of aggregates. Selected pixels corresponding to the Gaussian distributions identified in the N and B histograms in panels *a–c* are shown in Fig. 1 *d*. In this binary selection map, pixels corresponding to the green and red distributions are highlighted by the same color code. Pixels in the green distribution are located in the medium away from cells, whereas pixels in the red distribution (with higher brightness) are located at the membrane.

To better visualize our results, in Fig. 1, *e* and *f*, we show the B map and the average intensity map, respectively. The average intensity map shows a uniform concentration of nonaggregated molecules in the medium and a higher local concentration of native protein and aggregates at the membrane.

When we analyzed the data stacks acquired as a function of time, we obtained B-versus-intensity plots similar in shape to that shown in Fig. 1 *a*. Higher concentrations of molecules are always detected at the membrane, where progressive increase of brightness as a function of time is measured.

The time evolution of the average B (after subtraction of 1) of the red-selected distribution is reported in Fig. 2 *a*, i.e., pixels with intensity > 2.2. For data acquired at $t = 10$ min (Fig. 2 *b*), the center of this distribution is at $B = 1.32$, which corresponds to small aggregates composed of ~3 units. Fig. 2 *c* shows that these pixels are located at the membrane. For each time point, we observe a distribution of B-values ranging from B corresponding to single protein molecules ($B = 1.12$) to the B corresponding to larger aggregates. The increase in the average B-value (i.e., mean size of the aggregates) as a function of time indicates the progressive growth of aggregates.

After ~1 h, the B-value stops increasing. This may be explained by considering that aggregated proteins at the membrane could become progressively immobile, and that B for immobile molecules is always equal to one, because there is no variance attributable to particle fluctuations other than shot noise. Fig. 3 *a* shows the B-versus-intensity histogram of the data set relative to the measure at 100 min. The blue rectangle is used to select pixels with $B = 1$. These pixels are all localized at the membrane (see Fig. 3 *b*). The total number of these pixels with $B = 1$ can be calculated for each data set, and it increases as a function of time (data not shown). The presence of nonaggregated protein in the culture medium is always detected, and it is used as an internal reference for brightness.

A comparison of Fig. 1 *a* and Fig. 3 *a* shows that the overall intensity of the image decreases. This is not due to bleaching but to a reduction in the number of molecules in the region of interest (ROI). The progressive aggregation process may occur at the membrane of other cells in the dish and cause a reduction in the total number of molecules diffusing in the sample.

The simultaneous observation of cell morphology shows progressive shrinking of the cell and, after ~2 h, its death, as discussed further below.

The same experiment was repeated several times on both MEF and human breast cancer cells, at different protein

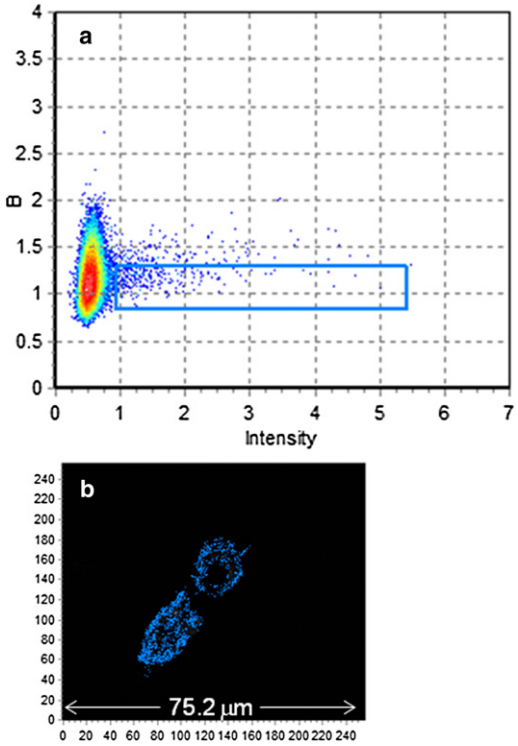

FIGURE 3 (*a*) B versus intensity histogram for data acquired 100 min after extracellular addition of ConA. The blue rectangle is used to select pixels with high intensity and B = 1 (immobile fraction) and highlight them in the selection map reported in panel *b*.

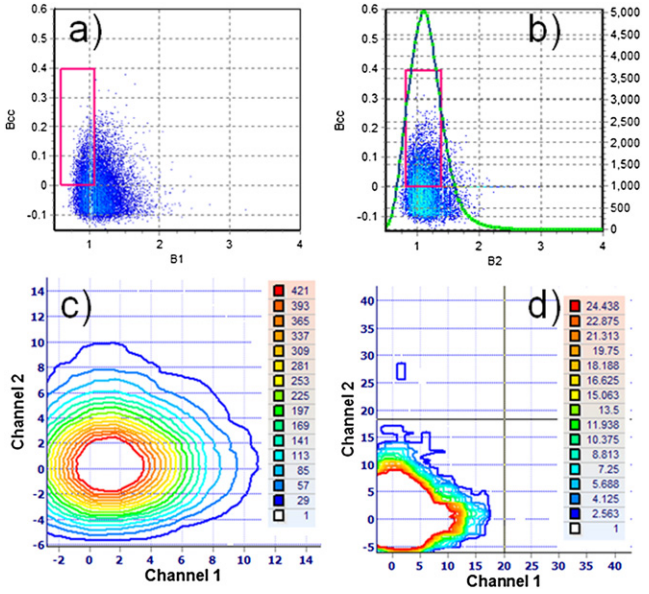

FIGURE 4 (*a*) Bcc versus B1 plot for an image stack acquired ~1 h after ConA extracellular addition. (*b*) Bcc versus B2 plot for the same image stack. Bcc plots show a region of brightness with positive cross-variance selected by the rectangular cursor. The green line in the Bcc2 plot shows the number of pixels with a given value of brightness as selected for B1 and for all positive values of B2. The maximum values of the green lines are reported in the stoichiometry plot, which shows the number of pixels with a given composition. (*c*) Stoichiometry contour plot relative to the ROI on the cell. (*d*) Stoichiometry contour plot relative to the ROI in the medium away from cell. In these contour plots, the brightness of channels 1 and 2 normalized with respect to calibration is reported. The contour lines (whose color is coded in the legend) correspond to the number of pixels that have a given pair of values of B1 and B2.

concentrations ranging from 90 to 300 nM with ConA labeled with Alexa647 or Alexa488, and using mixtures of labeled and unlabeled ConA. We observed analogous behaviors in the two cell types, but with different rates. In particular, progressive cell compaction and death were always observed to parallel aggregation as monitored by the increase of brightness.

Of interest, extracellular addition of mature ConA fibrils to the cell cultures at the same concentrations (data not shown) did not have a detectable effect, and there was no evidence of interaction between the fibril and the cell membrane.

Stoichiometry of protein aggregates: cross-N&B

The above data indicate that ConA oligomers are formed at the membrane as a function of time. To measure their stoichiometry while avoiding the contribution of the immobile fraction, we performed a cross-variance N&B analysis (26). This method provides pixel-resolution maps of molecular complexes and their stoichiometry from simultaneous fluctuations of the fluorescence intensity in two channels. Because only the contribution of correlated brightness in the two channels is taken into account, the impact of background noise on the analysis is reduced (26).

A solution containing ConA labeled with Alexa488 and Alexa647 was dissolved in the culture dish at 100 nM protein concentration, and the aggregation kinetics was followed as a function of time. The complexes and their stoichiometry were analyzed via a cross-brightness Bcc plot.

Fig. 4, *a* and *b*, show the Bcc1 and Bcc2 plots for an image stack acquired ~1 h after ConA extracellular addition. Bcc1 and Bcc2 are used to monitor and quantify interactions between ConA molecules labeled with the two dyes measured in separate channels. In this plot, pixels with uncorrelated fluctuation (i.e., where no interacting molecules are present) are close to the horizontal axis, whereas pixels with positive cross variances indicate the presence of proteins in a complex. A symmetric plot around the Bcc zero line would indicate the absence of interactions between proteins in the two channels because this would give, on average, the same number of positive and negative contributions to cross variance (see Fig. S1, *c* and *d*). Pixels with positive cross variances indicate the presence of proteins in a complex (26). As can be seen, the plots in Fig. 4, *a* and *b*, are not symmetric and are broadened toward positive values of Bcc, confirming the presence of protein complexes. In the Bcc plot, the height of a point on the vertical axis is proportional to the square of the product of the fluctuations occurring simultaneously in both channels;

therefore, pixels corresponding to higher points in the vertical axis correspond to larger aggregates.

The simultaneous selection of different pixel clusters from these plots gives information on the presence of complexes with a given brightness. Using a coincidence analysis algorithm, the SimFCS program explores the positive part of the variance plot for every pixel value with a given B1, identifying the corresponding value of B2, and provides a contour plot representing populations of pixels with a given combination of B (stoichiometry of aggregates) in the two channels. The *x-y* axes of the contour plot are normalized using the B1 and B2 values from the calibration (see Materials and Methods) and are expressed in multiples of the unit brightness values. Specifically, the Bcc1 plot in Fig. 4 *a* is explored for positive correlations. The green line in the Bcc2 plot (Fig. 4 *b*) shows the number of pixels with a given value of brightness as selected for B1 and for all positive values of B2. The operation is repeated for all locations in the Bcc1 plot by moving the cursor (*red rectangle*) along the horizontal axis. The maximum value of the green lines is reported in the contour plot that shows the number of pixels with a given composition. For example, a value of 2 (*red* or *green channel*) corresponds to a complex with two molecules. In brightness units, the combinations of B in channel 1 (ConA-Alexa488) and channel 2 (ConA-Alexa647) that give a number of pixels in the ROIs are shown. In the z axis, each contour line (coded in the legend) corresponds to the number of pixels that have a given pair of values of B1 and B2.

The stoichiometry histograms determined for an ROI located on the cell membrane and an ROI in the medium are reported in Fig. 4, *c* and *d*, respectively, and provide simultaneous information on the different processes occurring in the two areas. The contour plot in Fig. 4 *b* indicates that at the membrane there is a wide distribution of oligomers ranging from complexes formed from 2 to 20 units. The observed contour plot is approximately symmetric, indicating that, on average, an equal number of ConA-Alexa488 and ConA-Alexa647 molecules contribute to the complexes. At the same time, the same analysis (using the same calibration) in the ROI away from the cell membrane shows that a few larger aggregates are detected in only in a small number of pixels. Cross-N&B analysis verified that small ConA oligomers are found at the membrane, which allowed us to accurately quantify their stoichiometry. In line with the results obtained by single-color N&B experiments, we note that in ~50% of pixels in the considered ROI, oligomers are formed on average from <10 subunits (five green and five red).

Diffusion and binding of the aggregates: RICS

The RICS approach enabled us to measure ConA aggregate formation at the cell membrane, and to distinguish between the diffusion and binding processes that occurred during the observation time. This method can be used to measure diffusion of molecules in different ROIs and obtain detailed information about the location of the observed molecular process (28,29). RICS analysis can distinguish diffusion from binding processes by the shape of spatial autocorrelation function (30), which is different in the case of pure diffusion and in the case of rapid diffusion to fixed locations of binding (if its characteristic time is longer than the time a molecule takes to transit the point spread function) (30). If there are freely diffusing molecules and molecules undergoing binding-unbinding processes, the RICS function will yield a spatiotemporal correlation curve that is the linear combination of each type of molecule weighted by the square of the relative intensities. Therefore, RICS can distinguish whether binding processes are occurring.

The RICS analysis of data acquired at 100 min after ConA-Alexa647 addition in a selected region on the cell surface is shown in Fig. 5. The data can be analyzed using either the diffusion model or the binding model as described previously (30).

In Fig. 5, *a* and *c*, we show the RICS function calculated on a 64 $\times$ 64 ROI on the cell surface without and with subtraction of the immobile part, respectively. A round shape of the RICS function is shown in Fig. 5 *a*. This shape is given by immobile molecules on the membrane whose contribution is eliminated by means of an immobile subtraction algorithm. The immobile subtraction algorithm eliminates the contribution to fluctuations of particles residing at the same site for several frames. This suggests that the binding time is very long with respect to the frame time. In the analyses, the number of frame averages used for the immobile subtraction is indicated by the moving average (MAV). The length of the MAV needed to eliminate the contribution of immobile molecules can be useful to emphasize processes on different timescales, and in particular to select the slow processes that change the RICS autocorrelation function. Given the experimental conditions (frame time = 1.2 s), a MAV value of 10 corresponds to a residence time of ~10 s. The fitting of the RICS function after immobile subtraction using the diffusion model better describes the data in the selected ROI with respect to the fit obtained with the diffusion model without subtracting the immobile part. The diffusion coefficient was D = 16 $\pm$ 1 $\mu m^2/s$, which is compatible with small ConA aggregates diffusing in this area. We also show in Fig. 5, *e–g*, the RICS function obtained for an ROI outside the cell. The correlation function is described by a purely diffusive model (D = 40 $\pm$ 2 $\mu m^2/s$), and immobile subtraction does not affect its shape. The D-value outside the cell is compatible with the presence of nonaggregate protein or very small aggregates diffusing in the medium (the molecular weight of the ConA tetramer is 104,000, which gives $D_{ConA} = 46 \mu m^2/s$ in water at room temperature according the Stokes-Einstein equation).

In Fig. 6 we show the RICS autocorrelation function calculated for a different 64 $\times$ 64 pixel ROI selected on

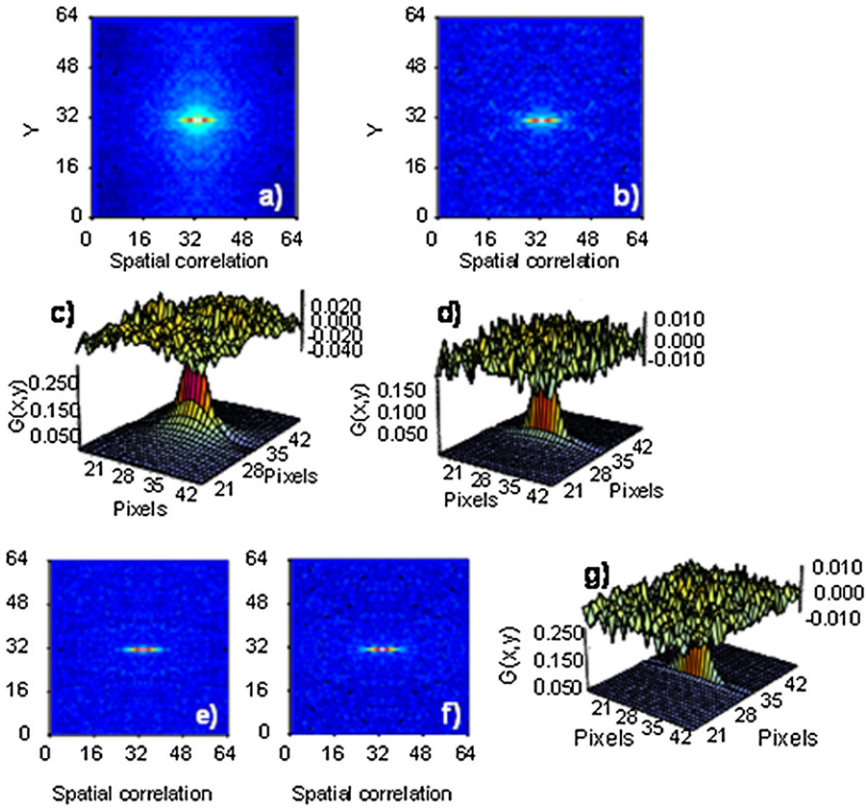

FIGURE 5 Spatial autocorrelation (RICS) function calculated without (*a*) and with (*b*) subtraction of the immobile fraction (MAV = 10) in a 64 × 64 pixel ROI. Cells were imaged at 256 × 256 pixels, scan speed 12.5μs/pixel, and the analysis was performed in the ROI on the cell. (*c*) Fit of the correlation function shown in *a*. The values of the amplitude of the correlation function and the diffusion coefficient are $G_0 = 0.30 \pm 0.05$ and $D = 4.3 \pm 0.5$ $\mu m^2/s$, respectively. (*d*) The fit of the correlation function shown in *b* with the diffusion model gives $G_0 = 0.18 \pm 0.03$ and $D = 16 \pm 1$ $\mu m^2/s$. (*e* and *f*) RICS in a 64 × 64 pixel ROI selected away from cells calculated without and with subtraction of the immobile fraction (MAV = 10). The two functions do not show appreciable differences. (*g*) The fit of the RICS function with the diffusion model gives $G_0 = 0.33 \pm 0.06$ and $D = 40 \pm 2$ $\mu m^2/s$.

the cell by varying the MAV. We analyzed these data using both the diffusion model and the binding model, and the characteristic parameters of the fits are reported in Table 1. As shown in the figure, the larger effect on changing the shape of the correlation function is observed for MAV = 4. This can be interpreted to mean that the processes related to binding-unbinding of the molecules occur slowly, on the 4 s timescale.

By repeating the analysis in different ROIs located at the membrane, we were able to distinguish regions where

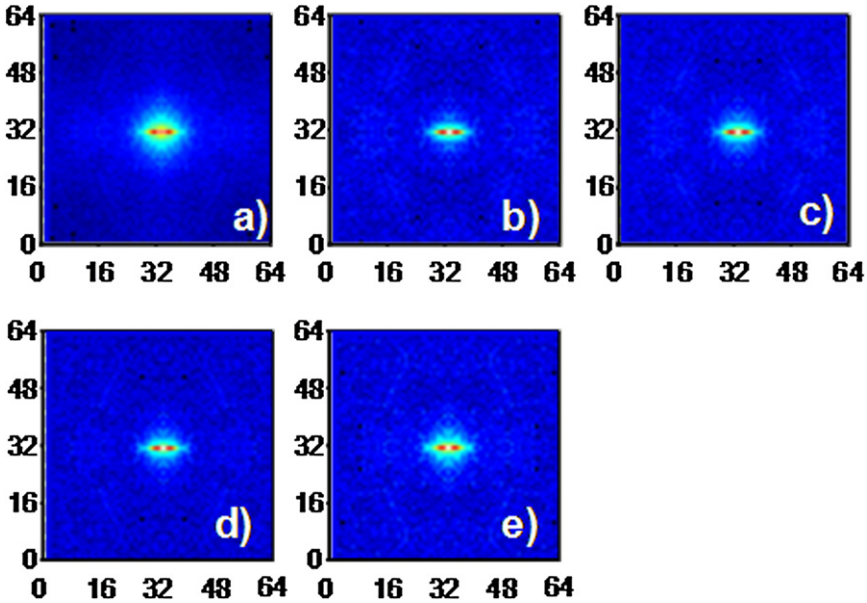

FIGURE 6 Spatial autocorrelation function calculated for a 64 × 64 pixel ROI on the cell surface. (*a*) Without subtracting the immobile fraction. (*b*) Subtracting the immobile fraction with MAV = 4, MAV = 10 (*c*), MAV = 20 (*d*), and MAV = 40 (*e*).

TABLE 1 Characteristic parameters obtained from the fit of the autocorrelation function after subtraction of different MAVs (from MAV = 4 to MAV = 40)

MAV = 4	MAV = 10	MAV = 20	MAV = 40
$G_0 = 0.18 \pm 0.01$	$G_0 = 0.22 \pm 0.01$	$G_0 = 0.23 \pm 0.01$	$G_0 = 0.23 \pm 0.01$
$D = 9\ \mu m^2/s \pm 0.8$	$D = 6.7\ \mu m^2/s \pm 0.7$	$D = 6.6\ \mu m^2/s \pm 0.7$	$D = 5.1\ \mu m^2/s \pm 0.4$
$A = 0.17 \pm 0.01$	$A = 0.20 \pm 0.01$	$A = 0.22 \pm 0.01$	$A = 0.22 \pm 0.01$
$\tau = 9$ ms ± 1	$\tau = 12$ ms ± 1	$\tau = 13$ ms ± 1	$\tau = 16$ ms ± 1

Values of the amplitude of the correlation function (G_0) and the diffusion coefficient D are calculated with the diffusion model, whereas A and τ are calculated with the binding model. The latter two parameters depend on the inverse number of binding sites and the on-off binding time, respectively (30).

aggregates were diffusing, and regions where the majority of the molecules were bound for an extended period of time. We report in Fig. 7 the RICS analysis performed on another ROI of the same cell. The RICS functions calculated without (*a*) and with (*b*) immobile subtraction (MAV = 10) are shown. The subtraction of the immobile fraction again changes the shape of the autocorrelation function, but the narrowing effect is less evident than the one observed for the data in Fig. 5, *a* and *b*. The analysis with the diffusion model, as reported in Fig. 7 *c*, yields $D = 7 \pm 1\ \mu m^2/s$. However, this model does not accurately describe our data, as can be seen from the quality of the fit; therefore, the estimation of the diffusion coefficient in this region is probably affected by the presence of a larger number of particles bound to the surface with respect to the area analyzed before. This apparent diffusion coefficient is probably affected by binding events occurring on a faster timescale (~50 ms). The shape of the RICS function narrows at the top and is smaller than the point spread function, and appears to be deformed toward a roundish shape that is more compatible with the binding process (30). Better results (and fit) are obtained when the analysis is repeated using the diffusion and binding model illustrated in Fig. 7 *d*. We estimated the diffusion coefficient and binding time at $D = 20 \pm 2\ \mu m^2/s$ and $\tau = 35 \pm 4$ ms, respectively. The analysis of different ROIs at the cell membrane (using the same MAV subtraction, MAV = 10) gives different diffusion coefficients ranging from 3 $\mu m^2/s$ to 25 $\mu m^2/s$, confirming that an ensemble of oligomers of different sizes is diffusing close to the cell. We note that the autocorrelation function obtained here is due to a linear combination of diffusion and binding functions, and that the binding-unbinding processes seem to be characterized by a time ranging from 10 ms to 50 ms.

Effects on cell membrane: Annexin V and Laurdan GP image measurements

We assessed the apoptotic behavior of cells by performing an Annexin V test. Annexin V is a protein that selectively binds phosphatidylserine (PS) after exposure during the early stages of apoptosis (9). Annexin-V binding to cell membranes has been shown to be a hallmark for detecting apoptotic cells. Fig. 8 *a* shows the morphology of Annexin V-fluorescein-stained MEF cells after treatment with 100 nM ConA for 3 h. Untreated cells are shown as controls in panel *b*. As indicated by the fluorescence signal, Annexin V binds cells treated with ConA, which also show the characteristic morphology of dying cells. Annexin V does not bind/stain (within experimental error) control cells, which also do not show changes in morphology.

In Fig. 9 the Laurdan GP images of cells taken 10 min (*a*) and 110 min (*b*) after addition of 100 nM ConA are shown together with their histograms in panel *c* (*blue* and *red plot*, respectively). The time evolution of the GP average value and its standard deviation (SD) are also shown in panels *d* and *e*, respectively. Fig. 9 shows a dramatic change in cell morphology indicating cell compaction and death. Moreover, as shown in Fig. 9, *d* and *e*, a progressive reduction in the

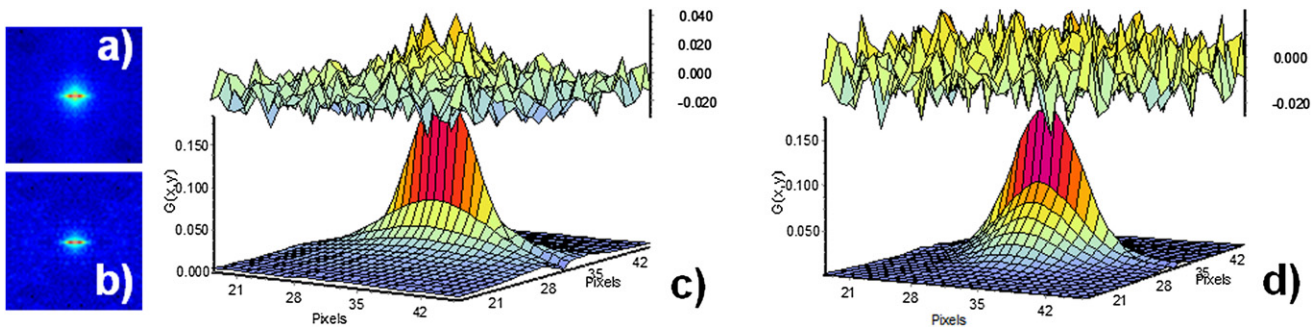

FIGURE 7 Spatial autocorrelation function (RICS) calculated for a 64 × 64 pixel ROI on the cell surface without subtraction (*a*) and with subtraction of the immobile fraction using MAV = 10 (*b*). (*c*) Fit of the correlation function shown in *b* using the diffusion model gives $G_0 = 0.19 \pm 0.6$ and $D = 7 \pm 1\ \mu m^2/s$. (*d*) Fit of the correlation function shown in *b* using a linear combination of the diffusion and binding models gives $G_0 = 0.090 \pm 0.01$, $D = 20 \pm 2\ \mu m^2/s$, and $A = 0.094 \pm 0.01$, $\tau = 35 \pm 4$ ms.

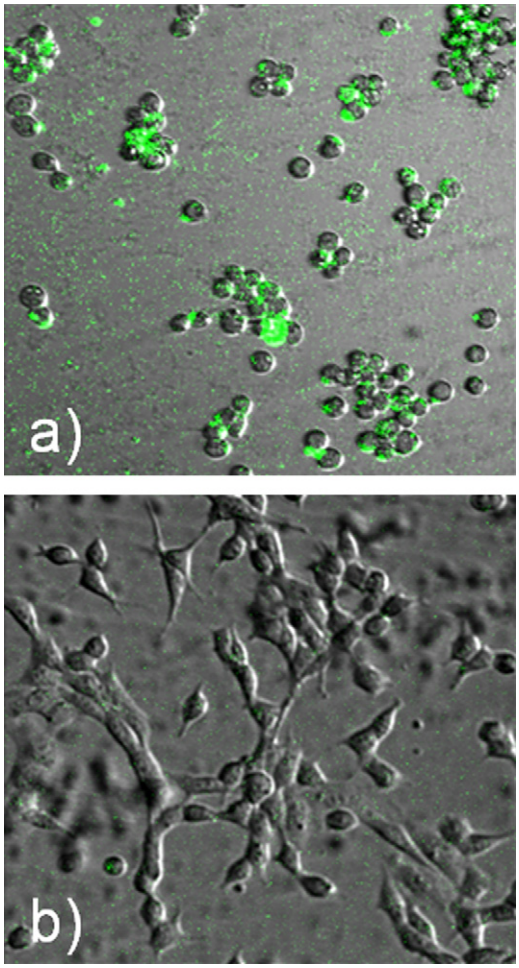

FIGURE 8 Morphology of Annexin-V-Fitc-stained MEF cells treated with ConA. (*a*) Cells incubated with 100 nM ConA for 3 h. AnnexinV-Fitc binds the cell surface, indicating apoptotic behavior. Phase-contrast and fluorescence images are superimposed. (*b*) Untreated cells are shown as controls: no AnnexinV-Fitc binding is observed in the same experimental conditions when cells are not treated with ConA.

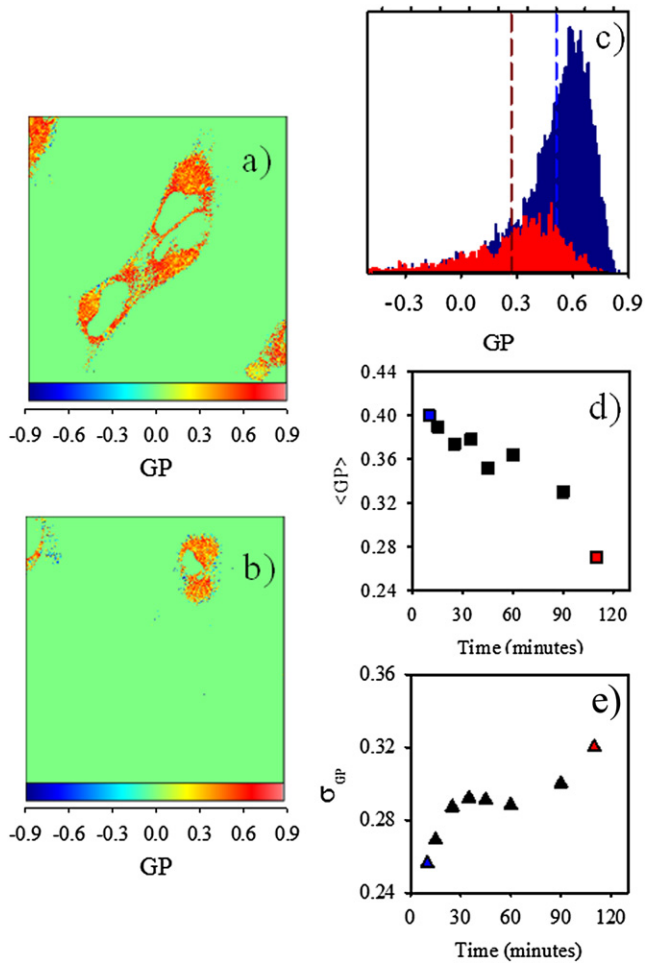

FIGURE 9 (*a*) Laurdan GP image of MEF cells acquired 10 min after extracellular addition of 100 nM ConA. (*b*) GP image of MEF cells acquired 110 min after extracellular addition of 100 nM ConA. (*c*) GP histograms of the two images (*blue plot*, relative to image acquired at 10 min; *red plot*, relative to image acquired at 110 min). (*d*) GP average values for similar images acquired as a function of time. (*e*) GP SD as a function of time.

average GP value is detected as a function of time together with an increase in the SD, which reflects the width of the GP distribution in the image. The GP average value reports on the level of water penetration into the membrane, which is related to packing of the lipids, whereas the width of the GP distribution is used as an indicator of the level of heterogeneity in the membrane organization (33). These data suggest that after ConA addition, during the same time interval in which ConA aggregation at the membrane is observed, the membrane is also damaged.

DISCUSSION

Our goal in this work was to examine common mechanisms that are thought to be involved in aggregation-related cytotoxicity. One of the advantages of fluctuation spectroscopy methods is that they enable one to observe protein aggregation in live cells, thus revealing the kinetics of the process as well as the location in the cell where aggregation occurs. This provides a more realistic view of aggregation occurring under physiological conditions than can be achieved by classical experiments in solution. For our studies, we chose ConA as a model because this protein is known to readily form fibrils within minutes under physiological conditions (21–23).

By combining the N&B and RICS methods, and using two colors, we were able to observe the ConA aggregation process occurring at the cell membrane and to establish the size of the protein oligomers. This approach provides a general methodology to investigate the onset and kinetics of protein aggregation directly in live cells, and allows one to determine the stoichiometry of the aggregates without invasive measurements.

After extracellular addition of ConA, we observed the progressive formation of a heterogeneous distribution of

small ConA aggregates (from 2 to ~10 proteins) at the membrane after a few minutes. Simultaneously, we were able to monitor the morphology of the cells and their progressive changes, compaction, and death. The B histogram distinguishes the presence of at least two different populations of molecules in the sample: nonaggregate proteins (ConA tetramers) diffusing in the medium away from the cells, and higher aggregates of protein at the cell membrane. This observation supports the idea that aggregation is favored by higher local concentration of the molecule at the membrane. Moreover, at the membrane, cross-N&B analysis allowed us to quantify the stoichiometry of the aggregates and confirmed the formation of small oligomers (mainly $<$10 proteins). This was also confirmed by RICS analysis, which also showed that binding-unbinding processes occur at the membrane in random locations. In line with results of the N&B analysis, the RICS analysis in different regions on the membrane or away from the cell indicated that the aggregation process occurs at the cell surface and is negligible in regions away from the membrane.

As observed for other cell lines (16–19,21) and confirmed here by the Annexin V test, extracellular addition of ConA causes cell death via an apoptotic pathway. We found that the structural organization of the membrane was progressively destroyed after ConA addition under the same conditions and in about the same time in which we observed progressive ConA aggregation at the membrane.

Taken together, our data indicate that the cell surface may provide nucleation sites for ConA aggregation where higher local concentrations favor the process. As previously suggested for other proteins (38–41), damage mechanisms may be initiated in this region. Small oligomers may interact with the membrane because of the exposure of reactive regions in partially unfolded proteins and the progressive formation of cross-β structures. This may stimulate generic cellular responses that perturb the membrane enough to cause cell death. It may be that large amyloids cannot perturb the membrane (and sufficiently reactive regions are recruited for the formation of the mature fibrillar structure), and for this reason they are harmless.

Our study also supports the use of image fluctuation techniques for studying a wide range of aggregation processes in both intracellular (26) and extracellular environments. These methods may provide new and detailed insights into the mechanisms involved in aggregation-related pathologies, and help elucidate the roles played by different aggregated species (e.g., amyloid aggregates, prefibrillar species, and transient oligomers) as toxic agents.

SUPPORTING MATERIAL

A detailed description of the materials and methods and two figures are available at http://www.biophysj.org/biophysj/supplemental/S0006-3495 S0006-3495(10)05223-9.

This work was supported in part by the Cell Migration Consortium (grant U54 GM064346 to M.D. and E.G.) and the National Institutes of Health (grants P41-RRO3155 and P50-GM076516 to G.O. and E.G.).

REFERENCES

1. Bucciantini, M., E. Giannoni, …, M. Stefani. 2002. Inherent toxicity of aggregates implies a common mechanism for protein misfolding diseases. *Nature.* 416:507–511.
2. Rochet, J.-C., and P. T. Lansbury, Jr. 2000. Amyloid fibrillogenesis: themes and variations. *Curr. Opin. Struct. Biol.* 10:60–68.
3. Walsh, D. M., I. Klyubin, …, D. J. Selkoe. 2002. Naturally secreted oligomers of amyloid β protein potently inhibit hippocampal long-term potentiation in vivo. *Nature.* 416:535–539.
4. Ross, C. A., and M. A. Poirier. 2004. Protein aggregation and neurodegenerative disease. *Nat. Med.* 10 (*Suppl*):S10–S17.
5. Dobson, C. M. 2003. Protein folding and misfolding. *Nature.* 426: 884–890.
6. Morozova-Roche, L. A., V. Zamotin, …, M. P. Kirpichnikov. 2004. Fibrillation of carrier protein albebetin and its biologically active constructs. Multiple oligomeric intermediates and pathways. *Biochemistry.* 43:9610–9619.
7. Cleary, J. P., D. M. Walsh, …, K. H. Ashe. 2005. Natural oligomers of the amyloid-β protein specifically disrupt cognitive function. *Nat. Neurosci.* 8:79–84.
8. Andersson, K., A. Olofsson, …, E. Lundgren. 2002. Only amyloidogenic intermediates of transthyretin induce apoptosis. *Biochem. Biophys. Res. Commun.* 294:309–314.
9. Gharibyan, A. L., V. Zamotin, …, L. A. Morozova-Roche. 2007. Lysozyme amyloid oligomers and fibrils induce cellular death via different apoptotic/necrotic pathways. *J. Mol. Biol.* 365:1337–1349.
10. Sirangelo, I., C. Malmo, …, G. Irace. 2004. Fibrillogenesis and cytotoxic activity of the amyloid-forming apomyoglobin mutant W7FW14F. *J. Biol. Chem.* 279:13183–13189.
11. Zamotin, V., A. Gharibyan, …, L. A. Morozova-Roche. 2006. Cytotoxicity of albebetin oligomers depends on cross-β-sheet formation. *FEBS Lett.* 580:2451–2457.
12. Ferreira, S. T., M. N. Vieira, and F. G. De Felice. 2007. Soluble protein oligomers as emerging toxins in Alzheimer's and other amyloid diseases. *IUBMB Life.* 59:332–345.
13. Lashuel, H. A. 2005. Membrane permeabilization: a common mechanism in protein-misfolding diseases. *Sci. SAGE KE.* 2005:pe28.
14. Lee, E. N., S. Y. Lee, …, S. R. Paik. 2003. Lipid interaction of α-synuclein during the metal-catalyzed oxidation in the presence of Cu^{2+} and H2O2. *J. Neurochem.* 84:1128–1142.
15. Engel, M. F. 2009. Membrane permeabilization by islet amyloid polypeptide. *Chem. Phys. Lipids.* 160:1–10.
16. Kulkarni, G. V., and C. A. G. McCulloch. 1995. Concanavalin A induced apoptosis in fibroblasts: the role of cell surface carbohydrates in lectin mediated cytotoxicity. *J. Cell. Physiol.* 165:119–133.
17. Cribbs, D. H., V. M. Kreng, …, C. W. Cotman. 1996. Cross-linking of concanavalin A receptors on cortical neurons induces programmed cell death. *Neuroscience.* 75:173–185.
18. Amin, A. R. M. R., R. K. Paul, …, M. L. Agarwal. 2007. A novel role for p73 in the regulation of Akt-Foxo1a-Bim signaling and apoptosis induced by the plant lectin, Concanavalin A. *Cancer Res.* 67:5617–5621.
19. Liu, B., C. Y. Li, …, J. K. Bao. 2009. Antiproliferative activity and apoptosis-inducing mechanism of Concanavalin A on human melanoma A375 cells. *Arch. Biochem. Biophys.* 482:1–6.
20. Anderson, A. J., C. J. Pike, and C. W. Cotman. 1995. Differential induction of immediate early gene proteins in cultured neurons by β-amyloid (A β): association of c-Jun with A β-induced apoptosis. *J. Neurochem.* 65:1487–1498.

21. Vetri, V., C. Canale, …, M. Leone. 2007. Amyloid fibrils formation and amorphous aggregation in concanavalin A. *Biophys. Chem.* 125: 184–190.

22. Vetri, V., F. Librizzi, …, M. Leone. 2007. Effects of succinylation on thermal induced amyloid formation in Concanavalin A. *Eur. Biophys. J.* 36:733–741.

23. Vetri, V., R. Carrotta, …, V. Militello. 2010. Concanavalin A aggregation and toxicity on cell cultures. *Biochim. Biophys. Acta.* 1804: 173–183.

24. Digman, M. A., R. Dalal, …, E. Gratton. 2008. Mapping the number of molecules and brightness in the laser scanning microscope. *Biophys. J.* 94:2320–2332.

25. Ossato, G., M. A. Digman, …, E. Gratton. 2010. A two-step path to inclusion formation of huntingtin peptides revealed by number and brightness analysis. *Biophys. J.* 98:3078–3085.

26. Digman, M. A., P. W. Wiseman, …, E. Gratton. 2009. Stoichiometry of molecular complexes at adhesions in living cells. *Proc. Natl. Acad. Sci. USA.* 106:2170–2175.

27. Dalal, R. B., M. A. Digman, …, E. Gratton. 2008. Determination of particle number and brightness using a laser scanning confocal microscope operating in the analog mode. *Microsc. Res. Tech.* 71:69–81.

28. Digman, M. A., C. M. Brown, …, E. Gratton. 2005. Measuring fast dynamics in solutions and cells with a laser scanning microscope. *Biophys. J.* 89:1317–1327.

29. Digman, M. A., P. Sengupta, …, E. Gratton. 2005. Fluctuation correlation spectroscopy with a laser-scanning microscope: exploiting the hidden time structure. *Biophys. J.* 88:L33–L36.

30. Digman, M. A., and E. Gratton. 2009. Analysis of diffusion and binding in cells using the RICS approach. *Microsc. Res. Tech.* 72:323–332.

31. Brown, C. M., R. B. Dalal, …, E. Gratton. 2008. Raster image correlation spectroscopy (RICS) for measuring fast protein dynamics and concentrations with a commercial laser scanning confocal microscope. *J. Microsc.* 229:78–91.

32. Digman, M. A., C. M. Brown, …, E. Gratton. 2008. Paxillin dynamics measured during adhesion assembly and disassembly by correlation spectroscopy. *Biophys. J.* 94:2819–2831.

33. Parasassi, T., E. Gratton, …, M. Levi. 1997. Two-photon fluorescence microscopy of Laurdan generalized polarization domains in model and natural membranes. *Biophys. J.* 72:2413–2429.

34. Bagatolli, L. A., E. Gratton, and G. D. Fidelio. 1998. Water dynamics in glycosphingolipid aggregates studied by Laurdan fluorescence. *Biophys. J.* 75:331–341.

35. Bagatolli, L. A., S. A. Sanchez, …, E. Gratton. 2003. Giant vesicles, Laurdan, and two-photon fluorescence microscopy: evidence of lipid lateral separation in bilayers. *Methods Enzymol.* 360:481–500.

36. Sánchez, S. A., M. A. Tricerri, and E. Gratton. 2007. Interaction of high density lipoprotein particles with membranes containing cholesterol. *J. Lipid Res.* 48:1689–1700.

37. Sánchez, S. A., M. A. Tricerri, …, E. Gratton. 2010. Lipid packing determines protein-membrane interactions: challenges for apolipoprotein A-I and high density lipoproteins. *Biochim. Biophys. Acta.* 7:1399–1408.

38. Shao, L., C. Dong, …, J. Ren. 2009. Studies on interaction of CdTe quantum dots with bovine serum albumin using fluorescence correlation spectroscopy. *J. Fluoresc.* 19:151–157.

39. Cecchi, C., S. Baglioni, …, M. Stefani. 2005. Insights into the molecular basis of the differing susceptibility of varying cell types to the toxicity of amyloid aggregates. *J. Cell Sci.* 118:3459–3470.

40. Stefani, M. 2007. Generic cell dysfunction in neurodegenerative disorders: role of surfaces in early protein misfolding, aggregation, and aggregate cytotoxicity. *Neuroscientist.* 13:519–531.

41. Engel, M. F. M., L. Khemtémourian, …, J. W. Höppener. 2008. Membrane damage by human islet amyloid polypeptide through fibril growth at the membrane. *Proc. Natl. Acad. Sci. USA.* 105:6033–6038.